


## RESEARCH ARTICLE

# Conjugated cobalt-based metal complex nanosheet for fabricating high-performance supercapacitor electrode

Qian Liu<sup>1</sup> | Zengqi Guo<sup>1</sup> | Zhiwei Xu<sup>1</sup> | Cong Wang<sup>1</sup> | Wai-Yeung Wong<sup>2</sup> 

<sup>1</sup>Anhui Province Key Laboratory of Functional Coordinated Complexes for Materials Chemistry and Application, School of Chemical and Environmental Engineering, Anhui Polytechnic University, Wuhu, People's Republic of China

<sup>2</sup>Department of Applied Biology and Chemical Technology and Research Institute for Smart Energy, The Hong Kong Polytechnic University, Hong Kong, People's Republic of China

## Correspondence

Qian Liu, Anhui Province Key Laboratory of Functional Coordinated Complexes for Materials Chemistry and Application, School of Chemical and Environmental Engineering, Anhui Polytechnic University, Wuhu 241000, People's Republic of China.  
Email: [lqcz\\_2008@ahpu.edu.cn](mailto:lqcz_2008@ahpu.edu.cn)

Wai-Yeung Wong, Department of Applied Biology and Chemical Technology and Research Institute for Smart Energy, The Hong Kong Polytechnic University, Hung Hom, Kowloon, Hong Kong, People's Republic of China.  
Email: [wai-yeung.wong@polyu.edu.hk](mailto:wai-yeung.wong@polyu.edu.hk)

## Funding information

Research Institute for Smart Energy (CDAQ) and Miss Clarea Au for the Endowed Professorship in Energy, Grant/Award Number: 847S; Anhui Provincial Demonstration Course Project "English for Science and Technology", Grant/Award Number: 2022qyw/sysfkc024; the RGC Senior Research Fellowship Scheme, Grant/Award Number: SRFS2021-5S01; Open Fund of Anhui Laboratory of Functional Coordinated Complexes for Materials Chemistry and Application, Grant/Award Number: LFCCMCA-04; the National Natural Science Foundation of China, Grant/Award Number: 51803002; Scientific Research Fund Project of the Nature Science Foundation of Anhui Province, Grant/Award Number: 1708085QE93; the Hong Kong Research Grants Council, Grant/Award Number: PolyU 15307321

## Abstract

In order to cope with the increasingly serious problem of energy shortage, supercapacitors have been developed as a clean and renewable energy source, and the supercapacitors with excellent energy density and long cycle life are imperative. Here, by employing a facile liquid–liquid (L–L) interfacial method at room temperature (RT), a set of two-dimensional (2D) metal complex nanosheets N1–N3 have been synthesized by the facile coordination between  $\text{Co}^{2+}$  ion and 2,3,6,7,10,11-hexaiminotriphenylene (HITP). Given the layered superstructure with well-ordered nanopores, the N1–N3 electrodes displayed excellent capacities of 4751.9, 5770.9 and 6075.2  $\text{F g}^{-1}$  at 1  $\text{A g}^{-1}$ , and a good cyclic stability with 92.1% capacity retention after 1000 cycles for the N3 electrode. The asymmetric supercapacitor device with N3 as the positive electrode delivers a maximum energy density of 238.2  $\text{Wh kg}^{-1}$  at a power density of 1610.1  $\text{W kg}^{-1}$  and an excellent cycling stability with a capacitance retention of 109.1% after 5000 cycles. This is the best electroactive bottom-up metal complex nanosheet reported so far for use in supercapacitor, which greatly expands the applicability of this 2D nanomaterial in energy device applications.

## KEYWORDS

2D nanosheet, bottom-up method, electrochemistry, specific capacitance, supercapacitor

This is an open access article under the terms of the [Creative Commons Attribution](https://creativecommons.org/licenses/by/4.0/) License, which permits use, distribution and reproduction in any medium, provided the original work is properly cited.

© 2024 The Author(s). *EcoMat* published by The Hong Kong Polytechnic University and John Wiley & Sons Australia, Ltd.

## 1 | INTRODUCTION

Mankind remains perplexed by energy shortage and environmental pollution problems which become constraints to the social development since this century. Under this circumstance, energy storage units such as batteries and supercapacitors (SCs) have attracted much attention, in which SCs are regarded as promising candidates owing to their high energy density, fast charge/discharge kinetics, relatively small volume, and excellent cycling stability.<sup>1–5</sup> SCs can be divided into electric double layer capacitors (EDLCs) and pseudocapacitors (PCs) on the basis of their storage mechanisms, which involve charge separation on the electrode surface for EDLCs, and Faradaic reactions on the surface or electrode-electrolyte interface for PCs, respectively. Generally, EDLCs own good conductivity but show inherent low capacitance, while PCs show high capacitance but have poor conductivity, hindering the electron transfer and leading to low capacitance at high current density.<sup>6</sup> Therefore, development of reliable electrode materials with good conductivity and high capacitance can be an effective way to overcome the above limitations.<sup>7</sup>

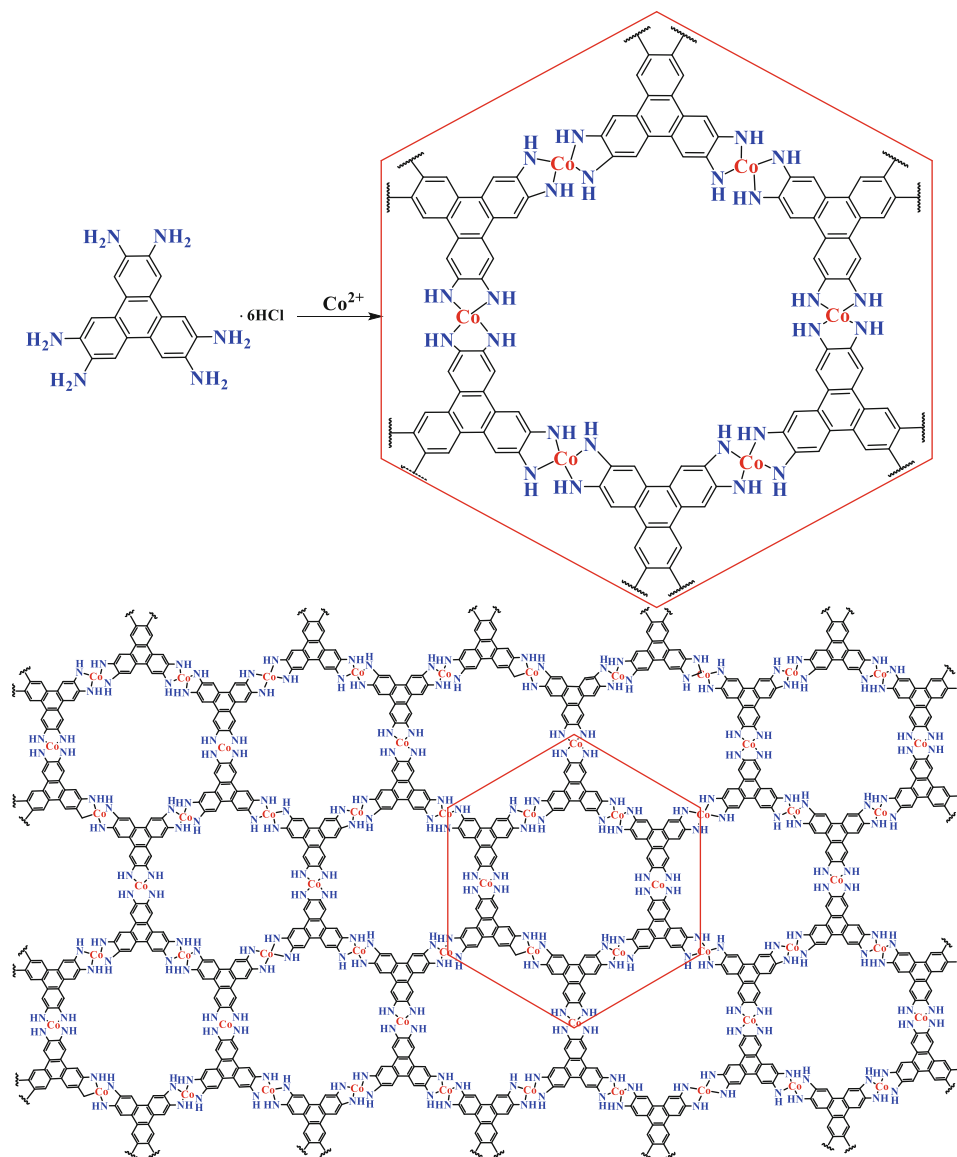
Since the first discovery of graphene in 2004, two-dimensional (2D) materials, for instance, silicone, phosphorene, metal oxides and metal hydroxides have been studied and extensively used in the domains of field-effect transistors, batteries and SCs.<sup>8–10</sup> As one of the best candidates to achieve high-performance supercapacitors, Pang and co-workers reported a 2D MXene based material, which was fabricated as symmetric SCs with areal capacitance of  $290.5 \text{ mF cm}^{-2}$  at  $1 \text{ mA cm}^{-2}$ , and stability over 10 000 cycles.<sup>11</sup> In particular, due to the rich redox activity of organic connectors as well as variable valence state of metal centres, 2D metal-organic frameworks (MOFs) with graphene-like structures have been shown to confer good conductivity, high surface area, and versatile functionalities, which are considered as promising electrodes for fabricating SCs. Hydrothermal synthesis and top-down exfoliation are the most common methods for getting 2D MOF materials according to the literature. For instance, Han and co-workers prepared a 2D conductive MOF (Ni-CAT) as a flexible independent membrane by combining the electrospinning technology with the hydrothermal method, which was used to fabricate a SC electrode and gave an energy density of  $18.67 \text{ Wh kg}^{-1}$  at a power density of  $297.12 \text{ W kg}^{-1}$ , and maintained 106.19% of the initial specific capacitance after 5000 cycles.<sup>12</sup> By the hydrothermal method, Wang et al. reported a Ni-MOF/CNTs, which was utilized as a positive electrode and delivered an energy density of  $36.6 \text{ Wh kg}^{-1}$  at a power density of  $480 \text{ W kg}^{-1}$ , as well as a good cycle life along with 95% specific capacitance retention after 5000 cycles.<sup>13</sup> Sun and co-workers

prepared a few-layer nanosheet  $\text{Ti}_3\text{C}_2\text{T}_x$  by the solvothermal intercalation and exfoliation method for supercapacitor applications, which displayed a specific capacity of  $508 \text{ F g}^{-1}$  at  $1 \text{ A g}^{-1}$  and an energy density of  $8.93 \text{ Wh kg}^{-1}$ .<sup>14</sup> Although hydrothermal process can effectively produce 2D materials, the high temperature condition causes severe aggregation of these nanomaterials. The properties of top-down nanosheets are also largely restricted by their mother materials. Furthermore, it is found that the energy density of SCs is governed by the morphology, size and microstructure of the electrode materials.<sup>15,16</sup> Thus, controllable synthesis of 2D MOF with uniform morphology and appropriate microstructure is crucial to improve its electrochemical performance as the SC electrode.

In the past decade, a new class of 2D MOF nanosheets have been fabricated directly from metal ions and organic ligands by the liquid-liquid (L-L) interfacial synthesis, from which the morphology and microstructure could be adjusted by selecting constituent building blocks (metal ions and organic ligands).<sup>17–19</sup> Besides, due to the in-plane delocalization via  $\pi$ -d conjugation realized by mixing the frontier orbitals of conjugated ligands and the d-orbitals of transition metals, 2D MOF nanosheets possess excellent electrical conductivity. For example, as a symmetric and conjugated ligand, HITP (2,3,6,7,10,11-hexamino triphenylene) can easily coordinate with metal ions ( $\text{Ni}^{2+}$ ,  $\text{Cu}^{2+}$ , etc) to form a metal-organic graphene analogue with good electrical conductivity,<sup>20,21</sup> which have been used in many fields such as chemiresistive sensing,<sup>21</sup> lithium-sulfur batteries,<sup>22</sup> electrocatalysts for oxygen evolution reaction<sup>23</sup> and fuel cell,<sup>24</sup> EDLC supercapacitor electrodes<sup>25</sup> and so on. In addition, such 2D MOF materials have good chemical stability. Bao et al. reported an electrode based on conductive hexaaminobenzene (HAB)-derived 2D MOFs, which not only possessed a high packing density and hierarchical porous structure, but also excellent chemical stability in both acidic and basic aqueous solutions.<sup>26</sup> Although numerous 2D nanomaterials have been constructed by amino derivatives, reports of bottom-up 2D nanosheets synthesized by the L-L interfacial method and used as electrodes of SCs are still very limited and this research needs to be further explored.

Given the above considerations, a group of 2D metal complex nanosheets N1-N3 have been synthesized by the facile coordination between  $\text{Co}^{2+}$  ion and HITP through a simple L-L interfacial method at room temperature. The as-fabricated N1-N3 have been used as electrodes which afforded excellent capacities of 4751.9, 5770.9 and  $6075.2 \text{ F g}^{-1}$  at  $1 \text{ A g}^{-1}$  respectively, and a good cycling stability with 92.1% capacity retention after 1000 cycles for the N3 electrode. The asymmetric supercapacitor (ASC) device was fabricated using N3 as the positive

**FIGURE 1** Schematic illustration and chemical structures of the nanosheets N1-N3 derived from  $\text{Co}^{2+}$  ion and its coordinated ligand HITP.



electrode and activated carbon (AC) as the negative electrode, delivering a maximum energy density of  $238.2 \text{ Wh kg}^{-1}$  at a current density of  $2 \text{ A g}^{-1}$  with a specific power of  $1610.1 \text{ W kg}^{-1}$ , accompanied by an outstanding cycling stability with a capacitance retention of 109.1% after 5000 cycles.

## 2 | RESULTS AND DISCUSSION

### 2.1 | Synthesis of nanosheets N1-N3 and referential complex P1

10 mL of degassed dichloromethane solution of the ligand HITP of three different concentrations ( $1.6 \times 10^{-5}$ ,  $3.2 \times 10^{-5}$ , and  $4.0 \times 10^{-5} \text{ mol L}^{-1}$ ) was each added into the glass bottles (50 mL capacity) with a diameter of 3.2 cm, respectively. After that, a buffer layer

was formed by covering with 10 mL of degassed D.I. water on the solutions. Then, 10 mL aqueous solution of  $\text{Co}(\text{NO}_3)_2 \cdot 6\text{H}_2\text{O}$  ( $0.05 \text{ mol L}^{-1}$ ) was injected into the mixture with a syringe. The reactions were carried out for 6 days at RT. After that, nanosheets with layered structure appeared at the L-L interface, which were marked as N1, N2 and N3, respectively (Figure 1). The as-fabricated nanosheets N1-N3 were transferred to the substrates and washed by D.I. water, ethanol, and dichloromethane, respectively, followed by drying under vacuum.

1.16 g of  $\text{Co}(\text{NO}_3)_2 \cdot 6\text{H}_2\text{O}$  was put into a degassed *N,N*-dimethylformamide solution of the HITP ( $2.4 \times 10^{-5} \text{ mol L}^{-1}$ , 80 mL), and the mixture was sonicated for 20 min to let the solid dissolve thoroughly. Then, the mixture was poured to a steel autoclave (100 mL capacity) with teflon-lined stainless steel. The reaction was done at  $160^\circ\text{C}$  for 12 h. Then the reaction

mixture was centrifuged with *N,N*-dimethylformamide several times to afford a purple precipitate, which was dried in vacuo for 12 h at 60°C and marked as P1.

## 2.2 | Structure and morphology of nanosheet N3

Through the L-L interfacial synthesis method, the ligand HITP with six functional amino groups could spontaneously coordinate with  $\text{Co}^{2+}$  to form the nanosheets N1-N3 with the topological structure depicted in Figure 1 (the counter anions are omitted for clarity). Here, in order to illustrate the advantages of bottom-up nanosheets, different solution concentrations of  $\text{Co}^{2+}$  ions were employed to give a set of nanosheets N1-N3, the electrochemical performances of which are all very impressive (vide infra). N1-N3 were insoluble in any organic solvents and water, facilitating its transfer to the substrates. FTIR spectrum of N3 is shown in Figure S1. The peaks at 3394.7, 1639.5, 1517.9 and 1433.1  $\text{cm}^{-1}$  can be assigned to the N—H stretching, N—H bending, aromatic C=C stretching and C—N stretching, respectively, which are all shifted compared with the ligand HITP, matching well with the features of  $\text{Co}^{2+}$  and HITP.<sup>26,27</sup> Furthermore, the presence of a new absorption band for Co-N stretching at 451.3  $\text{cm}^{-1}$  also confirms the coordination between amino nitrogen and  $\text{Co}^{2+}$ .<sup>28</sup> In order to study the crystallinity and phase purity, powder X-ray diffraction (PXRD) and theoretical simulation were conducted for nanosheet N3. As revealed from PXRD, nanosheet N3 displayed a strong diffraction peak at the  $2\theta$  value of 44.7°, which is assigned to the (021) plane and consistent with the result of the high resolution transmission electron microscopy (HRTEM) test (vide infra). The PXRD profile of the experimental pattern agrees with the simulated PXRD pattern of the AA-eclipsed stacking fairly well (Figure S2), suggesting that N3 has a structure of the AA-stacking model. The AA-stacking mode affords a unit cell with parameters of  $a = b = 39.83 \text{ \AA}$ ,  $c = 2.93 \text{ \AA}$ , and  $\alpha = \beta = 90^\circ$ ,  $\gamma = 120^\circ$  ( $R_{\text{wp}} = 3.17\%$ ,  $R_{\text{p}} = 2.03\%$ ). Table S1 shows the atomic coordinates for the AA-stacking mode of nanosheet N3. As shown in Figure 2A, the resultant gray nanosheet N3 completely covered the entire interface. The optical microscopy (OM) image (Figure 2B) shows a transparent gray colored N3 on a FTO substrate with a large domain size on one side exceeding 1 mm. The scanning electron microscopy (SEM) images also reveal a uniform, flat, film-like morphology for the nanosheet N3 (Figure 2C). The multilayer morphology on the edge reveals the layer-by-layer stacking for the bottom-up growth. To make a contrast, a traditional hydrothermal method was conducted to obtain a purple solid material P1 (Figure 2D).

SEM shows that P1 consists of aggregated small particles with an average particle size of  $3 \sim 4 \mu\text{m}$ , lacking of a continuous and well-distributed structure compared with the nanosheet N3 (Figure 2E). Furthermore, the atomic force microscopy (AFM) image of nanosheet N3 shows a flat and smooth sheet morphology for N3 (Figure 3A). The thickness of N3 was determined to be about 67.9 nm by analyzing the cross-section. The 3D AFM image also reveals its flat film morphology coverage on the Si substrate (Figure 3B). The TEM and HRTEM analyses were further conducted to study the detailed structure of the nanosheet N3. TEM image of N3 displays a clear 2D layered structure (Figure 3C) like a transparent silk scarf. The twisting and folding structure on the edge can provide the typical evidence of a 2D sheet material. Owing to the (021) crystal plane, a honeycomb hexagonal structure with a lattice fringe spacing of approximately 0.19 nm for N3 is clearly identified by the HRTEM image (Figure 3D,E), which is due to the interlayer distance of  $\pi$ - $\pi$  conjugated structure in N3, offering abundant redox sites and ion diffusion channels. The selected-area electron diffraction demonstrates the polycrystalline structure of N3 (inset of Figure 3D).

In order to detect the composition and distribution of elements, energy dispersive X-ray spectrometer (EDX) was conducted for the nanosheet N3. The SEM/EDX mapping images are given to reveal the homogeneity in the distribution of Co and N for N3 as proposed (Figure 3F-I). The obtained ratio of N:Co (3.27:1) is close to the ideal stoichiometric value (3:1) (Figure S3), revealing the successful coordination of  $\text{Co}^{2+}$  ion and amino groups into the nanosheet N3, which is consistent with the schematic illustration in Figure 1. X-ray photoelectron spectroscopy (XPS) was used to further investigate the internal structure and electronic surface state of N3, ligand HITP and referential complex P1 (Figure 4 and Figure S4). The peaks related to C 1s, N 1s, O 1s and Co 2p of N3 are shown in the spectrum (Figure 4A), and the existence of oxygen element likely arises from the air atmosphere. Compared with the ligand HITP (Figure S4A), an additional Co 2p peak is found for N3, demonstrating that  $\text{Co}^{2+}$  ion is bound to HITP. The valence state of Co ion in N3 has been confirmed to be only +2 (Figure 4B), while in P1, the valence states of Co ion are both +2 and +3 (Figure S4D). This is because some original  $\text{Co}^{2+}$  ions can be more prone to be oxidized to  $\text{Co}^{3+}$  ions at high temperature and pressure during the hydrothermal reaction. The binding energies at 780.8 eV and 796.6 eV match the Co 2p<sub>3/2</sub> and Co 2p<sub>1/2</sub> peaks for  $\text{Co}^{2+}$ , respectively.<sup>29,30</sup> In addition, the obvious satellite peak at 786.9 eV is related to the  $\text{Co}^{2+}$  resulting from the coordination between  $\text{Co}^{2+}$  and amino groups from the HITP.<sup>31</sup> In the presence of the Co(II)-N moieties and the C-N bond in the  $\pi$  conjugation group, the N 1s



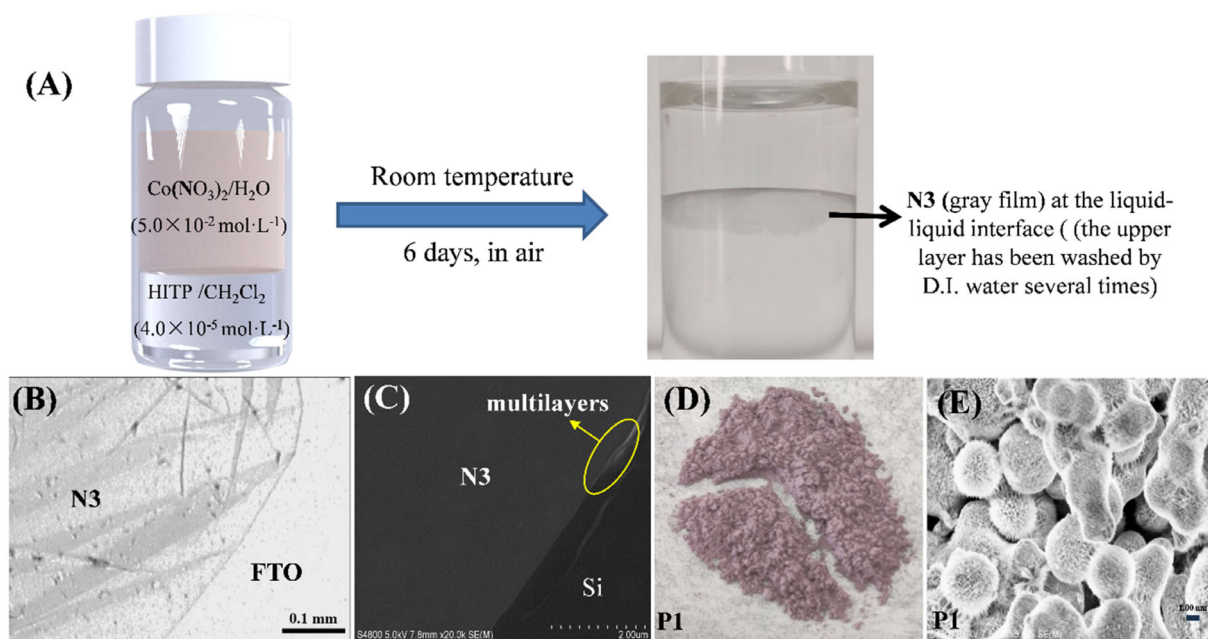


**FIGURE 2** (A) Schematic diagram and photo of the nanosheet N3 synthesized by the L-L interfacial method. (B) The OM image of the nanosheet N3 deposited on a FTO substrate. (C) The SEM image of the nanosheet N3 deposited on the Si substrate. (D) Photograph of the powder P1 from the reaction by hydrothermal method. (E) The SEM image of P1 on the Si substrate.

spectrum of N3 is deconvoluted into two peaks centered at 399.5 and 398.0 eV, respectively (Figure 4C).<sup>32,33</sup> The narrow scan XPS spectra focusing on the N 1s for ligand HITP, N3 and referential complex P1 can be found in Figure 4D. The peak of N 1s is shifted between HITP (397.6 eV) and N3 (398.3 eV) which shows a higher binding energy for N3, and demonstrates the coordination of functional amino groups of HITP with  $\text{Co}^{2+}$  ions to form N3. Furthermore, the disappearance of the shoulder peaks for N 1s is an indication of the completion of metal complexation.<sup>34</sup> In addition, the binding energy of N 1s core level for N3 is very similar to that of P1 (399.4 eV), which is a further proof for the formation of the Co(II)-N moieties within N3. Brunauer–Emmett–Teller (BET) tests were conducted for nanosheet N3 and referential complex P1 (Figure S5) to study their adsorption–desorption behavior. The specific surface areas of N3 and P1 are 39.67 and 16.71  $\text{m}^2 \text{g}^{-1}$ , respectively. This agrees with the concept that the mild L-L interfacial method for N3 is much more conducive to form a layered superstructure with ordered nanopores.

### 2.3 | Electrochemical performance of electrodes N1-N3 and P1

To ascertain the superiority of bottom-up nanosheets in the electrochemical performances, nanosheets N1-N3 with different ligand concentrations and referential complex P1 by hydrothermal method were prepared,

which were studied as positive electrodes, the electrochemical performances of which were evaluated by cyclic voltammetry (CV), galvanostatic charge–discharge (GCD), electrochemical impedance spectroscopy (EIS) and long-term stability measurements in a three-electrode system containing 1.0 M KOH aqueous solution.<sup>35</sup> The CV performances of electrodes N1-N3 and P1 at the scanning rates from 2 to 50  $\text{mV s}^{-1}$  are depicted in Figure 5A and Figure S6, respectively. Apparent redox peaks arise on the CV curves of all the N1-N3 electrodes, indicating that the pseudocapacitance behavior is attributed to the faradaic process on the electrode surface. The various oxidation states of cobalt and the possible conversion of cobalt in the possible charge and discharge mechanism are described in Equations S1 and S2.<sup>36</sup> As the scanning rate increases, the area of the CV curves and its peak value of the current density both significantly increase, demonstrating the rapid ion absorption and diffusion taking place in the electrodes N1-N3 and P1. Among these electrodes, the N1-N3 electrodes have higher integrated surface areas compared to P1 electrode in the potential window of 0 ~ 0.5 V at 10  $\text{mV s}^{-1}$  (Figure 5B), which indicates that the specific capacitances of N1-N3 prepared by the interfacial method are much better than that of P1 prepared by the solvothermal method. The uniform and continuous pore structure of nanosheets N1-N3 can give more electrochemical active sites, and hence reduce the ionic paths and enhance the electronic transport of the entire electrode material, which can also be proved by the larger

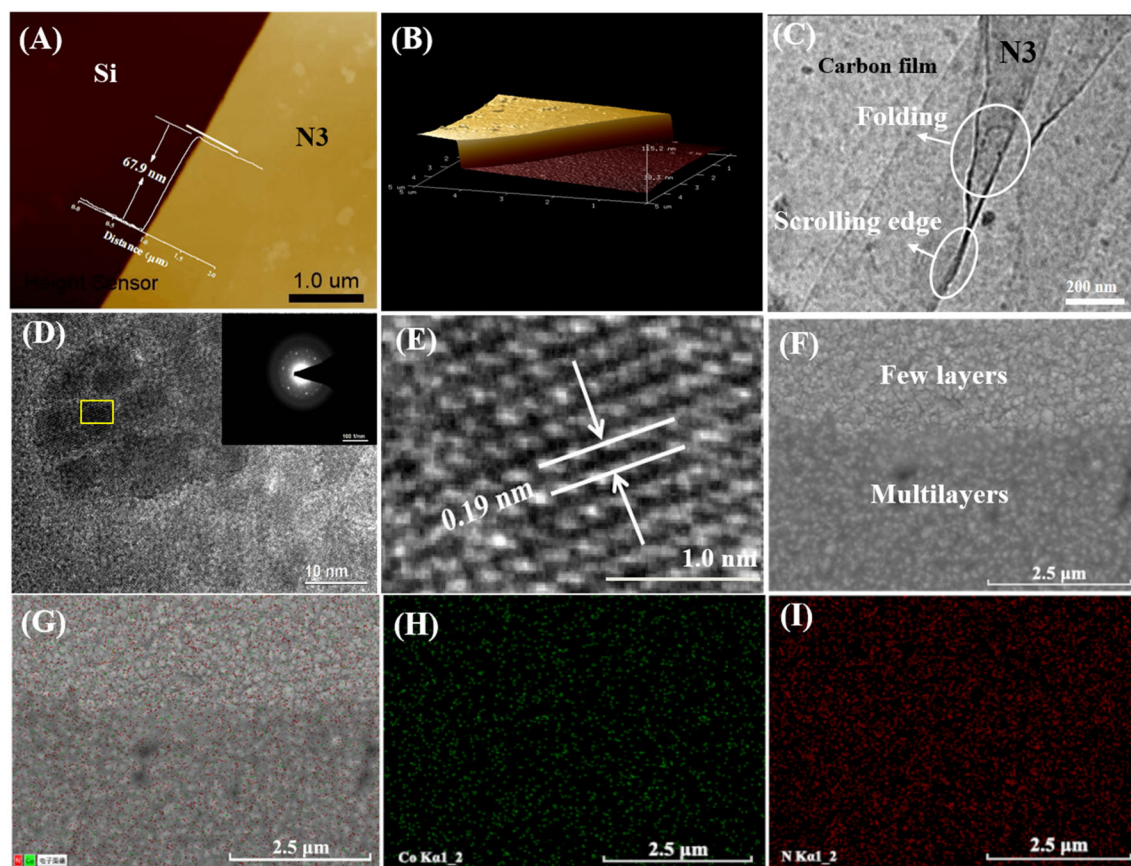


**FIGURE 3** (A) The AFM image of the nanosheet N3 and the cross-sectional analysis along with the white line. (B) The 3D AFM image of nanosheet N3. (C) TEM and (D) HRTEM image for N3 on ultrathin pure carbon film with no formvar backing on the lacey carbon support film. (E) The lattice distance of hexagonal structure shown in the yellow rectangle in (D). (F) The SEM/EDX of N3 on FTO substrate. The SEM/EDX mapping images of N3 for (G) Co, (H) N, (I) N, respectively.

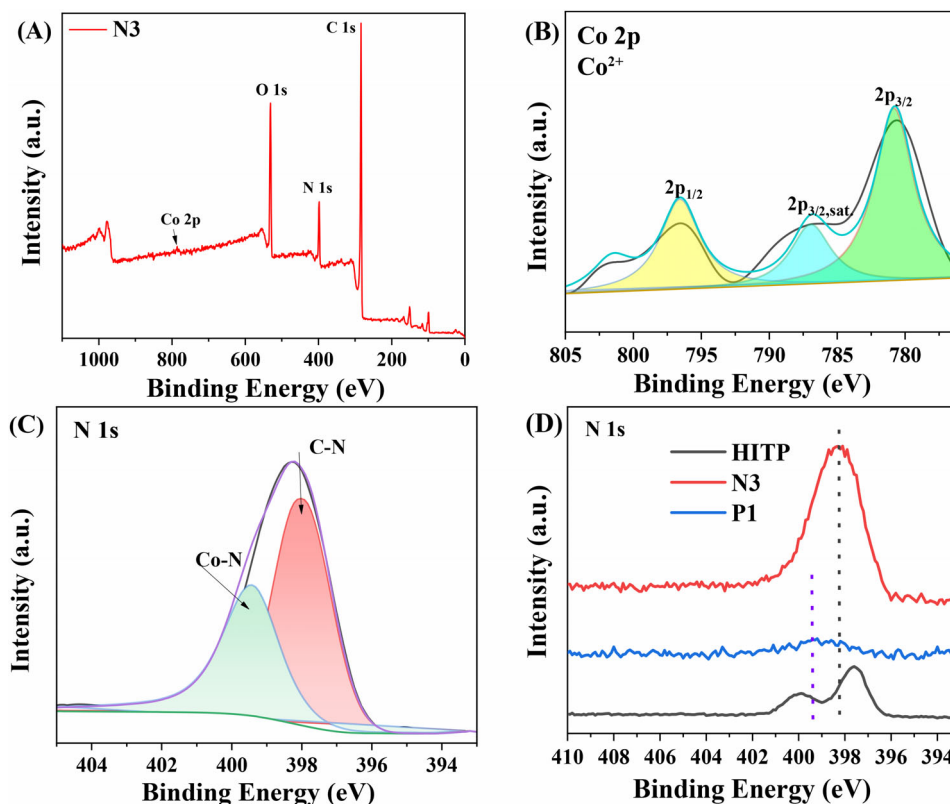
BET for electrode N3 compared to that of the electrode P1.<sup>37</sup>

To further clarify the charge storage dynamics of the electrodes N1–N3 and distinguish the surface-controlled capacitive behavior or diffusion-controlled process, the CV curves at different scanning rates have been analyzed for electrode N3 and the relationship between the peak current ( $i$ ) and scanning rate ( $v$ ) can be described by Formula S1 and logarithm peak current density ( $\log(i)$ ) and logarithm scanning rate ( $\log(v)$ ) were calculated by Formula S2. In general, values of 0.5 and 1 for  $b$  represent diffusion control processes and typical capacitance contribution, respectively.<sup>38</sup> The  $b$  values of the cathodic and anodic peaks are 0.62 and 0.64, indicating that the charge storage process in N3 is mainly controlled by a fast capacitive behavior (Figure 5C). Furthermore, the contribution of capacitive and diffusion-controlled charge storage to total charge storage can be quantified to study the charge storage mechanism according to Formula S3. The capacitive contribution for the electrode N3 accounts for 75.3% of the total capacitance at  $50 \text{ mV s}^{-1}$  (Figure 5D). As the scanning rate increases from 2 to  $50 \text{ mV s}^{-1}$ , the

capacitive contribution accordingly increases from 47.2% to 75.3% of the total capacitance, demonstrating that the charge storage for electrode N3 is mainly controlled by the Faradaic pseudocapacitive behavior rather than diffusion-controlled process (Figure 5E).

GCD curves of electrodes N1–N3 and P1 at the current densities of  $1 \sim 10 \text{ A g}^{-1}$  within the potential range of  $0 \sim 0.45 \text{ V}$  (Figure S7) demonstrate that the electrodes N1–N3 have good electrochemical capability. The shapes of charge–discharge curves do not conform to the characteristics of that of the isosceles triangle of electric double-layer behavior, which agrees with the characteristics of the CV curve mentioned above, thus also confirming that nanosheets N1–N3 can be used as the electrode materials of pseudocapacitive supercapacitors. At the current density of  $1 \text{ A g}^{-1}$ , the discharge times are 1995.8, 2423.8, and 2551.6 s for nanosheets N1–N3, but only 99.2 s for P1, which is far lower than that of N1–N3 (Figure 5F and Table 1). Figure 5G depicts a graph to intuitively reflect the capacitances of N1–N3 and P1 at different current densities. The high specific capacitance is caused by the ion exchange mechanism inside the material for

**FIGURE 4** (A) The full scan XPS spectrum of nanosheet N3. The narrow scan XPS spectra of N3 focusing on (B) Co 2p and (C) N 1s, respectively. (D) The narrow scan XPS spectra of ligand HITP, nanosheet N3 and referential complex P1 focusing on N 1s core level.



the pseudocapacitance.<sup>39</sup> When the current is lower, there is much more time for OH<sup>-</sup> to transfer between the electrodes' surface and the solution to be inserted into or extracted out of the electrode materials, which indicates that more charge could be transferred and stored to obtain higher specific capacitance. According to Formula S4, the specific capacitance values of 4751.9, 5770.9, and 6075.2 F g<sup>-1</sup> have been obtained for the electrodes N1-N3 at 1 A g<sup>-1</sup>, respectively (Table 1), which outperformed most other reported electrode materials (Figure 6 and Table S2). In addition, electrodes N1-N3 exhibit good symmetry under the conditions of different current densities, which indicates that N1-N3 have good reversibility and stability. At the same current density of 1 A g<sup>-1</sup>, only a value of 230.7 F g<sup>-1</sup> has been obtained for electrode P1, which is far lower than those of the N1-N3 electrodes. It can be seen that the nanosheets N1-N3 prepared by the L-L interfacial method show an enormous potential in the application of electrochemical energy storage because of their large specific surface area and abundant active centers available compared with P1 prepared by the hydrothermal method. From Figure 5H, the GCD tests of 1000 cycles were conducted to investigate the cycling stability of the nanosheet N3 electrode at 10 A g<sup>-1</sup> in the potential range of 0 ~ 0.45 V. The specific capacitance can be held steady at about 92.1% of the initial value from 800 cycles to 1000 cycles. Actually, from the 500th cycle

to the 1000th cycle, only a decrease of 1.1% can be observed. The inset in Figure 5F shows the typical GCD curves in the first three cycles and the last three cycles of the nanosheet N3. The similarity in the time-potential response behavior of each charge-discharge cycle indicates that each cycle process is reversible and the electrode material is stable.<sup>36</sup> EIS tests were also performed for nanosheet N3 and comparative sample P1. The EIS Nyquist plot is shown in Figure 5I for the N3 electrode, which consists of a tiny semicircle in the high frequency region and a straight line in the low frequency region. According to the point where the actual impedance (Z') axis intersects in the high frequency region, a very small electrolyte resistance  $R_s$  of 0.14  $\Omega$  represents that the resistance between the nanosheet N3 and electrolyte during the Faradic reactions is very low, indicating an excellent charge transfer performance for N3, which is also revealed by the semicircle ( $R_{ct} = 0.76 \Omega$ ) in the high frequency region. In the low frequency region, the inclination angle of the curved line is significantly greater than 45°, demonstrating the better ion mobility than that of P1 (<45°). This is because the appropriate interlayer distance of N3 and the micro/mesopore formed by the stacking of N3 can facilitate the migration of OH<sup>-</sup> ions. Compared to N3, the value of  $R_s$  for P1 (0.36  $\Omega$ ) is greater than that of the nanosheet N3 (0.14  $\Omega$ ), which suggests that the charge transfer for P1 is relatively lower.



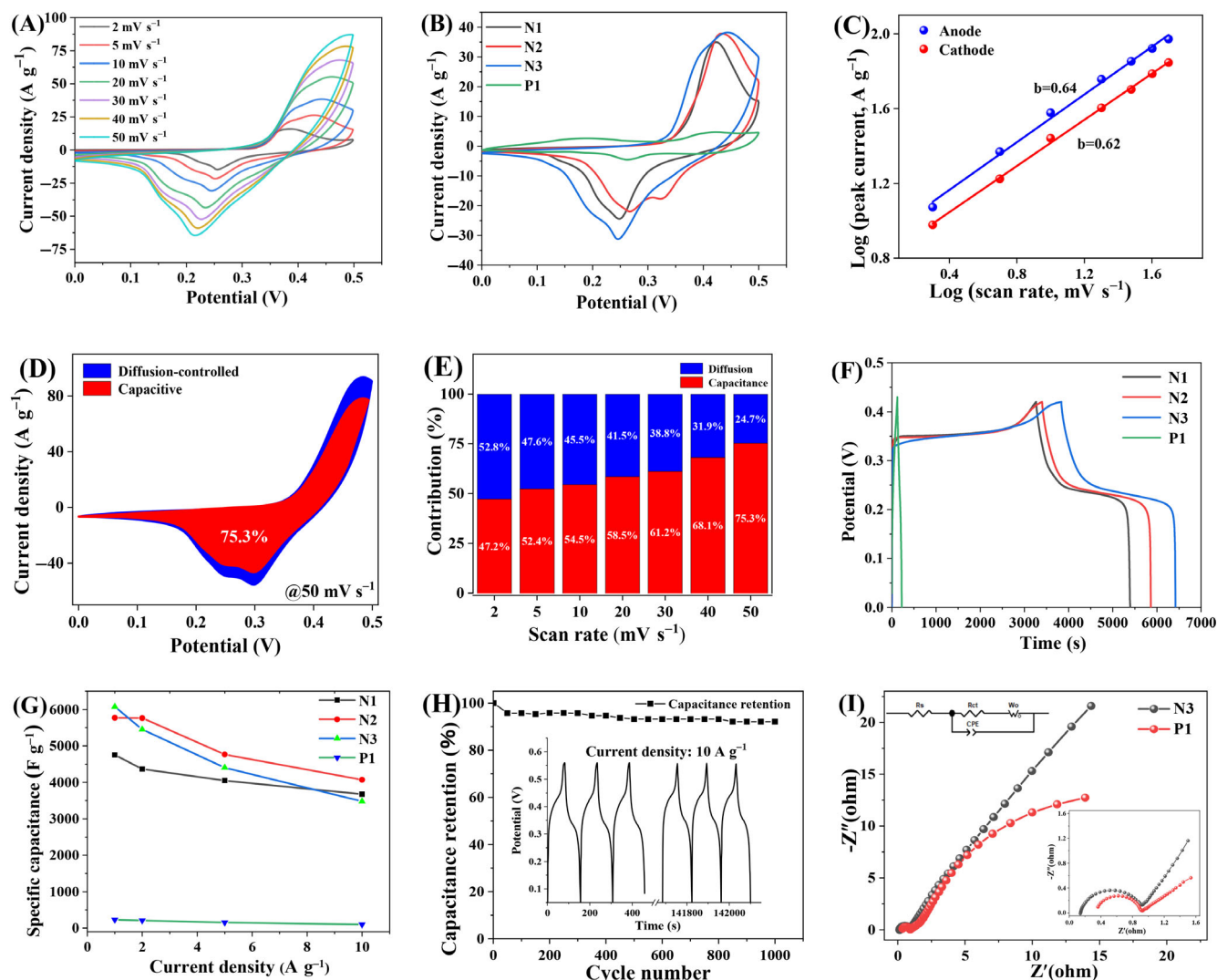


**FIGURE 5** (A) CV curves of the electrode N3 at different scanning rates. (B) The CV curves of various electrodes at  $10 \text{ mV s}^{-1}$ . (C) The  $b$ -value determination of the peak anodic and cathodic currents for N3. (D) Capacitance contribution at a scanning rate of  $50 \text{ mV s}^{-1}$  for N3. (E) Contribution of capacitive and diffusion-controlled percentages at different scanning rates from 2 to  $50 \text{ mV s}^{-1}$  for N3. (F) GCD curves of various electrodes at  $1 \text{ A g}^{-1}$ . (G) Specific capacitance curves of various electrodes at different current densities. (H) Cycling performance of the N3 electrode in the potential range of  $0 \sim 0.45 \text{ V}$  at  $10 \text{ A g}^{-1}$ . The inset shows the GCD processes for the first three cycles and the last three cycles. (I) Comparison of the EIS Nyquist plots for N3 and P1 electrodes. Inset: The high-frequency region data for (I).

**TABLE 1** Discharge times and specific capacitances for electrodes based on N1-N3 and P1 with current densities of 1, 2, 5 and  $10 \text{ A g}^{-1}$ .

Current density ( $\text{A g}^{-1}$ )	Discharge time (s)				Specific capacitance ( $\text{F g}^{-1}$ )			
	N1	N2	N3	P1	N1	N2	N3	P1
1	1995.8	2423.8	2551.6	99.2	4751.9	5770.9	6075.2	230.7
2	916.8	1210.6	1144.8	45.0	4365.7	5764.8	5451.4	209.3
5	340.0	400.4	370.0	13.4	4047.6	4766.7	4404.8	155.8
10	154.4	171.0	146.1	4.3	3676.2	4071.4	3478.6	100.0

## 2.4 | Electrochemical performance of N3//AC (active carbon) based asymmetric supercapacitor (ASC)

To further estimate the practical application of nanosheet N3 as electrode material, ASC device was prepared in

6 M KOH aqueous solution using N3 and AC as a positive electrode and negative electrode, respectively. The CV curve of AC in Figure 7A displays typical characteristics of a double layer supercapacitor with a rectangular closed area. The redox peak in the quasi-rectangular CV curves indicates the effectiveness of the integration of



pseudocapacitance and double-layer capacitance. In addition, there is no significant change in the shape of the CV curve as the scanning rate increases, demonstrating good stability and capacitance performance.<sup>40,41</sup> The GCD curves were conducted to give the charge/discharge

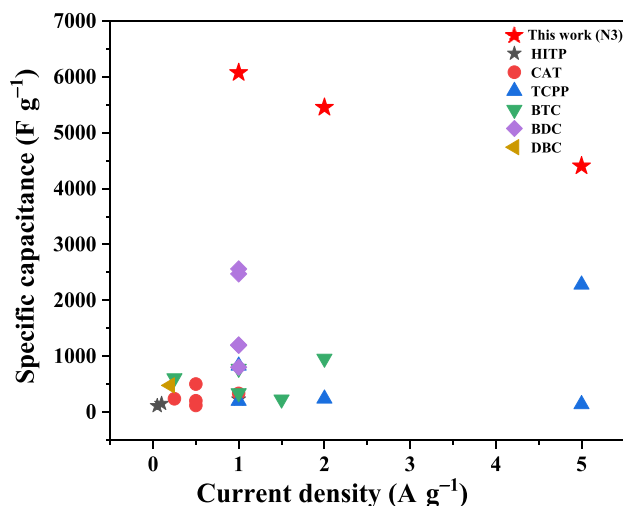


**FIGURE 6** Comparison of the specific capacitance for various materials with different typical ligands for previous literature reports and this work.

performance of the as-fabricated ASC device at different current densities (Figure 7C), which also reveals the pseudocapacitive behavior. The specific capacitance of the as-fabricated ASC device at different discharge current densities of 2, 4, 6, 8 and 10 A g<sup>-1</sup> were 670.0, 568.4, 470.7, 236.5 and 158.1 F g<sup>-1</sup>, respectively (Table S3). Due to the Faradaic reactions, the EIS Nyquist plot of the as-fabricated ASC device exhibits a semi-circle in the high frequency region (Figure 7D) and shows a very low  $R_s$  of 0.63  $\Omega$ , which is in accordance with the fact that the low internal resistance is beneficial for OH<sup>-</sup> ions to approach the active centers.<sup>42</sup> The specific energy of the as-fabricated ASC device is as high as 238.2 Wh kg<sup>-1</sup> at a current density of 2 A g<sup>-1</sup> with a specific power of 1610.1 W kg<sup>-1</sup>. As the current density is up to 10 A g<sup>-1</sup>, the specific energy can be maintained at 56.7 Wh kg<sup>-1</sup> with a specific power of 7996.8 W kg<sup>-1</sup> (Formulas S6 and S7), demonstrating a very high rate of charge-discharge for this as-fabricated ASC device, which can maintain both high power density and energy density. These values outperform those of most other reported ASC electrode materials, for instance, CNF@Ni-CAT//AC,<sup>12</sup> NMORP//AC,<sup>43</sup> NCP//AC,<sup>44</sup> NiTe//AC,<sup>45</sup> Co<sub>3</sub>O<sub>4</sub>@NF//CNT@HCNF-1.5,<sup>46</sup> PCN//MXene,<sup>47</sup> Fe-Co-Ni MOF//AC,<sup>48</sup> PANI NWAs//Ti<sub>3</sub>C<sub>2</sub>TX,<sup>49</sup> Mn/NiCo-LDH//AC,<sup>50</sup>

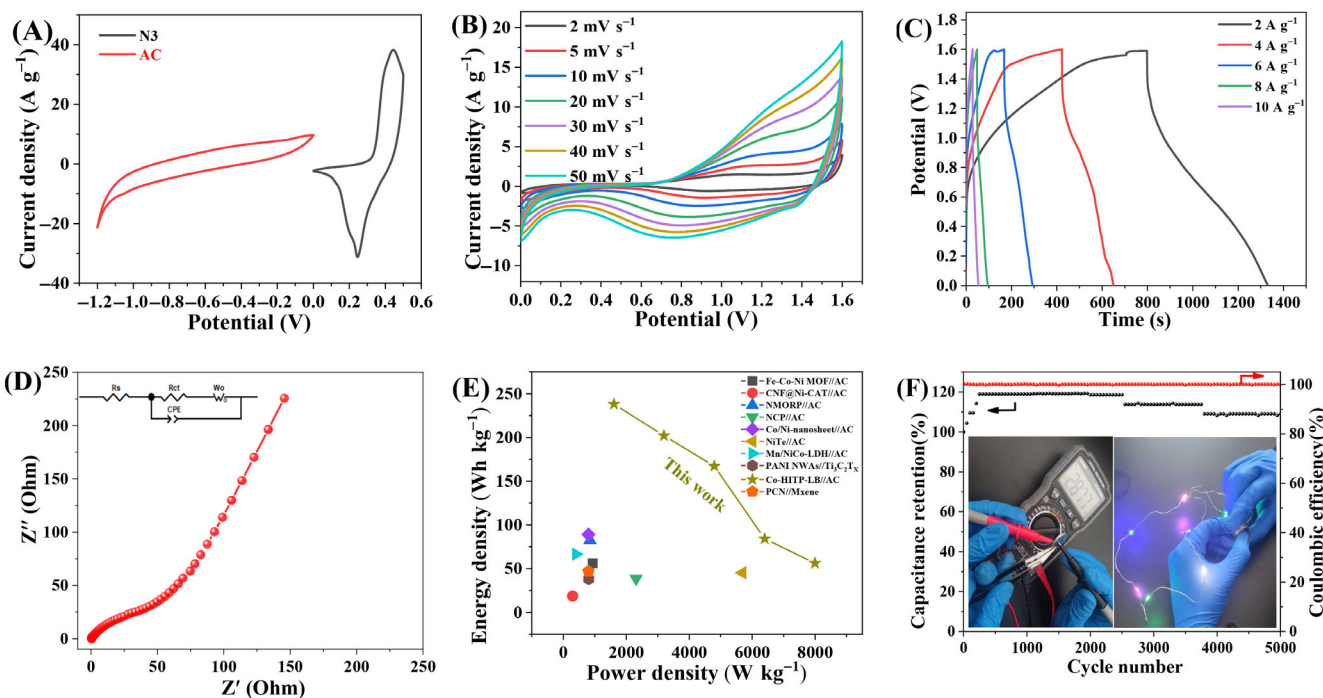


**FIGURE 7** (A) Comparison of CV curves between N3 and AC electrodes at 10 mV s<sup>-1</sup>. Electrochemical performances of N3//AC based ASC device (B) CV curves with different potentials at scanning rates from 2 to 50 mV s<sup>-1</sup>. (C) GCD curves at current densities from 2 to 10 A g<sup>-1</sup>. (D) EIS Nyquist plots for the ASC device. (E) Comparison of energy density and power density with other reported ASCs electrode materials. (F) Cycling stability and coulombic efficiency of N3//AC device at the current density of 10 A g<sup>-1</sup> after 5000 cycles. Inset: Sketch for lighting up the LEDs by N3//AC based ASC device.

CoNi-nanosheet//AC<sup>51</sup> (see Figure 7E). Additionally, the GCD tests of 5000 cycles were conducted to examine the cycling performance of N3//ASC device at 10 A g<sup>-1</sup> in the potential range of 0 ~ 1.6 V (Figure 7F). A significant upward trend for the specific capacitance is shown in the first 2000 cycles and 119.3% of the initial specific capacitance can be reached, which can be considered as an activation process in the initial cycle process. After 5000 cycles, the as-fabricated ASC device can still keep 109.1% of the original capacitance along with a coulombic efficiency of nearly 100%. LEDs can be illuminated for more than 10 min by connecting three as-fabricated ASC devices in series (inset of Figure 7F), testifying the potential value of N3 in energy device applications.

### 3 | CONCLUSION

A series of hexaiminotriphenylene ligand-based metal complex nanosheet N1-N3 have been successfully synthesized by a simple L-L interfacial method at RT. The as-prepared nanosheet N3 has been identified by FTIR, PXRD and simulation study, and OM, SEM, AFM and HRTEM images reveal a uniform, flat, film-like morphology for N3, which have a large domain size (>1 mm in one side) with a thickness of 67.9 nm. Compared with the referential complex P1, nanosheet N3 displays an efficient utilization rate of redox active sites and good energy storage performance, indicating the advantages of 2D metal complex nanosheet prepared by the bottom-up method. Nanosheets N1-N3 have been exploited as SC electrodes, showing excellent capacities of 4751.9, 5770.9 and 6075.2 F g<sup>-1</sup> at 1 A g<sup>-1</sup> respectively, and a good cycling stability with 92.1% capacity retention after 1000 cycles for N3. The N3//AC based ASC device displays a maximum energy density of 238.2 Wh kg<sup>-1</sup> at a power density of 1610.1 W kg<sup>-1</sup>, accompanied by an outstanding cycling stability with a capacitance retention of 109.1% after 5000 cycles, which is better than most other ASC electrode materials reported. This holds a great promise of exploiting the nanosheet N3 in energy-storage devices and obviously leads to a significant expansion of the applicability of such 2D nanomaterials in energy-related applications.

### ACKNOWLEDGMENTS

Q. L. thanks the National Natural Science Foundation of China (51803002), Scientific Research Fund Project of the Nature Science Foundation of Anhui Province (1708085QE93), Open Fund of Anhui Laboratory of Functional Coordinated Complexes for Materials Chemistry and Application (LFCCMCA-04), Anhui Provincial

Demonstration Course Project “English for Science and Technology” (2022qyw/sysfkc024). W. Y. W. is grateful to the financial support from the Hong Kong Research Grants Council (PolyU 15307321), the RGC Senior Research Fellowship Scheme (SRFS2021-5S01), Research Institute for Smart Energy (CDAQ) and Miss Clarea Au for the Endowed Professorship in Energy (847S).

### CONFLICT OF INTEREST STATEMENT

The authors declare no conflicts of interest.

### ORCID

Wai-Yeung Wong  <https://orcid.org/0000-0002-9949-7525>

### REFERENCES

- Li B, Hu N, Su Y, et al. Direct inkjet printing of aqueous inks to flexible all-solid-state graphene hybrid micro-supercapacitors. *ACS Appl Mater Interfaces*. 2019;11(49):46044-46053. doi:10.1021/acsami.9b12225
- Feng M, Zhang Y, Zhu X, Chen W, Lu W, Wu G. Interface-anchored covalent organic frameworks@amino-modified Ti<sub>3</sub>C<sub>2</sub>T<sub>x</sub> MXene on nylon 6 film for high-performance deformable supercapacitors. *Angew Chem Int ed*. 2023;62(33):e202307195. doi:10.1002/anie.202307195
- Liu T, Yan R, Huang H, et al. A micromolding method for transparent and flexible thin-film supercapacitors and hybrid supercapacitors. *Adv Funct Mater*. 2020;30(46):2004410. doi:10.1002/adfm.202004410
- Zheng S, Xue H, Pang H. Supercapacitors based on metal coordination materials. *Coord Chem Rev*. 2018;373:2-21. doi:10.1016/j.ccr.2017.07.002
- Liu CL, Bai Y, Li WT, Yang F, Zhang G, Pang H. In situ growth of three-dimensional MXene/metal-organic framework composites for high-performance supercapacitors. *Angew Chem Int ed*. 2022;61(11):e202116282. doi:10.1002/anie.202116282
- Zeng L, Lou X, Zhang J, Wu C, Liu J, Jia C. Carbonaceous mudstone and lignin-derived activated carbon and its application for supercapacitor electrode. *Surf Coat Techn*. 2019;357:580-586. doi:10.1016/j.surfcoat.2018.10.041
- Wang Y, Liu Y, Wang H, et al. Ultrathin NiCo-MOF nanosheets for high-performance supercapacitor electrodes. *ACS Appl Energy Mater*. 2019;2(3):2063-2071. doi:10.1021/acsaem.8b02128
- Novoselov KS, Geim AK, Morozov SV, et al. Electric field effect in atomically thin carbon films. *Science*. 2004;306(5696):666-669. doi:10.1126/science.1102896
- Qin Z, Pan J, Lu S, et al. Direct evidence of dirac signature in bilayer germanene islands on Cu(111). *Adv Mater*. 2017;29(13):1606046. doi:10.1002/adma.201606046
- Molle A, Goldberger J, Houssa M, Xu Y, Zhang SC, Akinwande D. Buckled two-dimensional Xene sheets. *Nat Mater*. 2017;16(2):163-169. doi:10.1038/nmat4802
- Bai Y, Liu CL, Chen TT, et al. MXene-copper/cobalt hybrids via Lewis acidic molten salts etching for high performance symmetric supercapacitors. *Angew Chem Int ed*. 2021;60(48):25318-25322. doi:10.1002/anie.202112381

12. Zhao S, Wu H, Li Y, et al. Core-shell assembly of carbon nanofibers and a 2D conductive metal-organic framework as a flexible free-standing membrane for high-performance supercapacitors. *Inorg Chem Front*. 2019;6(7):1824-1830. doi:10.1039/C9QI00390H
13. Wen P, Gong P, Sun J, Wang J, Yang S. Design and synthesis of Ni-MOF/CNT composites and rGO/carbon nitride composites for an asymmetric supercapacitor with high energy and power density. *J Mater Chem A*. 2015;3(26):13874-13883. doi:10.1039/C5TA02461G
14. An H, Wang S, Liu K, et al. Preparation of polyaniline nanorods wrapped on solvothermal-exfoliated  $\text{Ti}_3\text{C}_2\text{T}_x$  as electrode materials for high-performance supercapacitors. *Colloids Interface Sci Commun*. 2022;50:100650. doi:10.1016/j.colcom.2022.100650
15. Salunkhe RR, Kaneti YV, Yamauchi Y. Metal-organic framework-derived nanoporous metal oxides toward supercapacitor applications: progress and prospects. *ACS Nano*. 2017;11(6):5293-5308.
16. Wang L, Shao D, Guo J, Zhang S, Lu Y. Superstable porous Coordination polymer as the electrode material for supercapacitor. *J Solid State Chem*. 2019;277:630-635. doi:10.1016/j.jssc.2019.06.039
17. Sakamoto R, Hoshiko K, Liu Q, et al. A photofunctional bottom-up bis(dipyrinato)zinc(II) complex nanosheet. *Nat Commun*. 2015;6(1):6373. doi:10.1038/ncomms7713
18. Liu Q, Guo Z, Wang C, et al. A cobalt-based metal-organic framework nanosheet as the electrode for high-performance asymmetric supercapacitor. *Adv Sci*. 2023;10(18):2207545. doi:10.1002/advs.202207545
19. Fang M, Xu L, Zhang H, Zhu Y, Wong WY. Metalloporphyrin-linked mercurated graphynes for ultrastable  $\text{CO}_2$  electroreduction to CO with nearly 100% selectivity at a current density of  $1.2 \text{ A cm}^{-2}$ . *J Am Chem Soc*. 2022;144(33):15143-15154. doi:10.1021/jacs.2c05059
20. Sheberla D, Sun L, Blood-Forsythe M, et al. High electrical conductivity in  $\text{Ni}_3(2,3,6,7,10,11\text{-hexaiminotriphenylene})_2$ , a semi-conducting metal-organic graphene analogue. *J Am Chem Soc*. 2014;136(25):8859-8862. doi:10.1021/ja502765n
21. Campbell MG, Liu SF, Swage TM, et al. Chemiresistive sensor arrays from conductive 2D metal-organic frameworks. *J Am Chem Soc*. 2015;137(43):13780-13783. doi:10.1021/jacs.5b09600
22. Zang Y, Pei F, Huang J, Fu Z, Xu G, Fang X. Large-area preparation of crack-free crystalline microporous conductive membrane to upgrade high energy lithium-sulfur batteries. *Adv Energy Mater*. 2018;8(31):1802052. doi:10.1002/aenm.201802052
23. Xing D, Wang Y, Zhou P, et al.  $\text{Co}_3(\text{hexaiminotriphenylene})_2$ : a conductive two-dimensional  $\pi$ -d conjugated metal-organic framework for highly efficient oxygen evolution reaction. *Appl Catal B Environ*. 2020;278:119295. doi:10.1016/j.apcatb.2020.119295
24. Chen X, Sun F, Bai F, Xie Z. DFT study of the two dimensional metal-organic frameworks  $\text{X}_3(\text{HITP})_2$  as the cathode electrocatalysts for fuel cell. *Appl Surf Sci*. 2019;471:256-262. doi:10.1016/j.apsusc.2018.12.014
25. Borysiewicz MA, Dou J-H, Stassen I, Dincă M. Why conductivity is not always king-physical properties governing the capacitance of 2D metal-organic framework-based EDLC supercapacitor electrodes: a  $\text{Ni}_3(\text{HITP})_2$  case study. *Faraday Discuss*. 2021;231:298-304. doi:10.1039/D1FD00028D
26. Feng D, Lei T, Lukatskaya MR, et al. Robust and conductive two-dimensional metal-organic frameworks with exceptionally high volumetric and areal capacitance. *Nat Energy*. 2018;3(1):30-36. doi:10.1038/s41560-017-0044-5
27. Lahiri N, Lotfizadeh N, Tsuchikawa R, Deshpande VV, Louie J. Hexaaminobenzene as a building block for a family of 2D coordination polymers. *J Am Chem Soc*. 2017;139(1):19-22. doi:10.1021/jacs.6b09889
28. Liang Y, Wei J, Hu Y, et al. Metal-polydopamine frameworks and their transformation to hollow metal/N-doped carbon particles. *Nanoscale*. 2017;9(16):5323-5328. doi:10.1039/C7NR00978J
29. Park J, Lee M, Feng D, et al. Stabilization of hexaaminobenzene in a 2D conductive metal-organic framework for high power sodium storage. *J Am Chem Soc*. 2018;140(32):10315-10323. doi:10.1021/jacs.8b06020
30. Yu H, Xie S, Yang J, et al.  $\text{Co}_3\text{Fe}_7/\text{Mo}_2\text{C}$  co-embedded in N-codoped porous carbon with accelerated kinetics for OER and HER. *Colloid Surface A*. 2022;645:128953. doi:10.1016/j.colsurfa.2022.128953
31. Martin BK, Bezerra LS, Artemkina S, et al. Efficient OER nanocomposite electrocatalysts based on Ni and/or Co supported on  $\text{MoSe}_2$  nanoribbons and  $\text{MoS}_2$  nanosheets. *Chem Eng J Adv*. 2022;9:100206. doi:10.1016/j.cej.2021.100206
32. Sanetuntikul J, Hyun S, Ganesan P, Shanmugam S. Cobalt and nitrogen co-doped hierarchically porous carbon nanostructure: a bifunctional electrocatalyst for oxygen reduction and evolution reactions. *J Mater Chem A*. 2018;6(47):24078-24085. doi:10.1039/C8TA08476A
33. Cheng D, Zhao Y, Tang X, et al. Densely integrated Co, N-Codoped graphene@carbon nanotube porous hybrids for high-performance lithium-sulfur batteries. *Carbon*. 2019;149:750-759. doi:10.1016/j.carbon.2019.04.108
34. Liu YR, Deng WW, Meng ZG, Wong WY. Dual-ion batteries: a tetrakis(terpyridine) ligand-based cobalt(II) complex nanosheet as a stable dual-ion battery cathode material. *Small*. 2020;16(17):2070092. doi:10.1002/smll.202070092
35. Sondermann L, Jiang W, Shviro M, et al. Nickel-based metal-organic frameworks as electrocatalysts for the oxygen evolution reaction (OER). *Molecules*. 2022;27(4):1241. doi:10.3390/molecules27041241
36. Liu X, Shi C, Zhai CW, Cheng M, Liu Q, Wang G. Cobalt-based layered metal-organic framework as an ultrahigh capacity supercapacitor electrode material. *ACS Appl Mater Interfaces*. 2016;8(7):4585-4591. doi:10.1021/acsami.5b10781
37. Asaithambi S, Sakthivel P, Karuppaiah M, et al. Synthesis and characterization of various transition metals doped  $\text{SnO}_2@-\text{MoS}_2$  composites for supercapacitor and photocatalytic applications. *J Alloys Compd*. 2021;853:157060. doi:10.1016/j.jallcom.2020.157060
38. Zhang P, Wang M, Liu Y, et al. Largely pseudocapacitive two-dimensional conjugated metal-organic framework anodes with lowest unoccupied molecular orbital localized in nickel-bis(dithiolene) linkages. *J Am Chem Soc*. 2023;145(11):6247-6256. doi:10.1021/jacs.2c12684
39. Liang J, Peng H, Wang ZM, et al. Rare earth metal lanthanum-organic frameworks derived three-dimensional mesoporous

- interconnected carbon nanosheets for advanced energy storage. *Electrochim Acta*. 2020;353:136597. doi:[10.1016/j.electacta.2020.136597](https://doi.org/10.1016/j.electacta.2020.136597)
40. Pu XL, Ren XH, Yin HF, Tang Y, Yuan H. One-step electrodeposition strategy for growing nickel cobalt hydroxysulfide nanosheets for supercapacitor application. *J Alloys Compd*. 2021;865:158736. doi:[10.1016/j.jallcom.2021.158736](https://doi.org/10.1016/j.jallcom.2021.158736)
  41. Zha D, Fu Y, Zhang L, Zhu J, Wang X. Design and fabrication of highly open nickel cobalt sulfide nanosheets on Ni foam for asymmetric supercapacitors with high energy density and long cycle-life. *J Power Sources*. 2018;378:31-39. doi:[10.1016/j.jpowsour.2017.12.020](https://doi.org/10.1016/j.jpowsour.2017.12.020)
  42. Hou R, Miao M, Wang Q, et al. Integrated conductive hybrid architecture of metal-organic framework nanowire array on polypyrrole membrane for all-solid-state flexible supercapacitors. *Adv Energy Mater*. 2020;10(1):1901892. doi:[10.1002/aenm.201901892](https://doi.org/10.1002/aenm.201901892)
  43. Fahad HM, Shaheen F, Ahmad R, Aziz MH, Ifseisi AA, Huang Q. A 3D hydrangea-like NiMoO<sub>4</sub>/rGO/PANI hybrid composite for high performance asymmetric supercapacitor. *Electrochim Acta*. 2024;477:143756. doi:[10.1016/j.electacta.2023.143756](https://doi.org/10.1016/j.electacta.2023.143756)
  44. Abazari R, Sanati S, Morsali A, Dubal DP. High specific capacitance of a 3D-metal-organic framework-confined growth in CoMn<sub>2</sub>O<sub>4</sub> nanostars as advanced supercapacitor electrode materials. *J Mater Chem A*. 2021;9(17):11001-11012. doi:[10.1039/D1TA00900A](https://doi.org/10.1039/D1TA00900A)
  45. Meghanathan KL, Parthibavarman M, Sharmila V, Joshua JR. Metal-organic framework-derived Nickel Tellurideporous structured composites electrode materials for asymmetric supercapacitor application. *J Energy Storage*. 2023;72:108665. doi:[10.1016/j.est.2023.108665](https://doi.org/10.1016/j.est.2023.108665)
  46. Li X, Zhang H, Lin ZT, et al. Cobalt-nickel coordinated polyaniline as electrodes for high performance flexible asymmetric supercapacitor. *J Energy Storage*. 2023;72:108266. doi:[10.1016/j.est.2023.108266](https://doi.org/10.1016/j.est.2023.108266)
  47. Kim T, Subedi S, Dahal B, et al. Homogeneous elongation of N-doped CNTs over nano-fibrillated hollow-carbon-nanofiber: mass and charge balance in asymmetric supercapacitors is no longer problematic. *Adv Sci*. 2022;9(20):2200650. doi:[10.1002/adv.202200650](https://doi.org/10.1002/adv.202200650)
  48. Farahani FS, Rahmanifar MS, Noori A, et al. Trilayer metal-organic frameworks as multifunctional electrocatalysts for energy conversion and storage applications. *J Am Chem Soc*. 2022;144(8):3411-3428. doi:[10.1021/jacs.1c10963](https://doi.org/10.1021/jacs.1c10963)
  49. Yu YF, Zhang HP, Xie YQ, et al. Vertically aligned graphene-MXene nanosheets based electrodes for high electrochemical performance asymmetric supercapacitor. *Chem Eng J*. 2024;482:149063. doi:[10.1016/j.cej.2024.149063](https://doi.org/10.1016/j.cej.2024.149063)
  50. Guo W, Dun C, Yu C, et al. Mismatching integration-enabled strains and defects engineering in LDH microstructure for high-rate and long-life charge storage. *Nat Commun*. 2022;13(1):1409. doi:[10.1038/s41467-022-28918-0](https://doi.org/10.1038/s41467-022-28918-0)
  51. Zhang YF, Han CM, Bai C, et al. Supercapacitors based on mixed nickel/cobalt 2D MOF coordination nanosheets for energy storage. *ACS Appl Nano Mater*. 2024;7(4):3897-3906. doi:[10.1021/acsanm.3c05513](https://doi.org/10.1021/acsanm.3c05513)

## SUPPORTING INFORMATION

Additional supporting information can be found online in the Supporting Information section at the end of this article.

**How to cite this article:** Liu Q, Guo Z, Xu Z, Wang C, Wong W-Y. Conjugated cobalt-based metal complex nanosheet for fabricating high-performance supercapacitor electrode. *EcoMat*. 2024;6(8):e12480. doi:[10.1002/eom2.12480](https://doi.org/10.1002/eom2.12480)